

Automated Cutting Plane Positioning for Intracranial Aneurysm Quantification

Tim Jerman , Aichi Chien , Franjo Pernuš, Boštjan Likar, and Žiga Špiclin 

Abstract—Objective: Aneurysm rupture risk can be assessed by its morphologic and hemodynamics features extracted based on angiographic images. Feature extraction entails aneurysm isolation, typically by manually positioning a cutting plane (MCP). To eliminate intra- and inter-rater variabilities, we propose automatic cutting plane (ACP) positioning based on the analysis of vascular surface mesh. **Methods:** Innovative Hough-like and multi-hypothesis-based detection of aneurysm center, parent vessel inlets, and centerlines were proposed. These were used for initialization and iterative ACP positioning by geometry-inspired cost function optimization. For validation and baseline comparison, we tested MCP and manual neck curve-based isolation. Isolated aneurysm morphology was characterized by size, dome height, aspect ratio, and nonsphericity index. **Results:** Methods were applied to 55 intracranial saccular aneurysms from two sites, involving 3-D digital subtraction angiography, computed tomography angiography, and magnetic resonance angiography modalities. Isolation based on ACP resulted in smaller average inter-curve distances (AICDs), compared to those obtained by MCP. One case had AICD higher than 1.0 mm, while 90% of cases had $AICD < 0.5$ mm. Intra- and inter-rater AICD variability of manual neck curves was higher compared to MCP, validating its robustness for clinical purposes. **Conclusion:** The ACP method achieved high accuracy and reliability of aneurysm isolation, also confirmed by expert visual analysis. So extracted morphologic features were in good agreement with MCP-based ones, therefore, ACP has great potential for aneurysm morphology and hemodynamics quantification in clinical applications. **Significance:** The novel method is angiographic modality agnostic; it delivers repeatable isolation important in follow-up aneurysm assessment; its performance is comparable to MCP; and re-evaluation is fast and simple.

Index Terms—Angiogram, intracranial aneurysm, cutting plane, neck curve, morphologic features, quantification.

Manuscript received February 2, 2019; revised May 13, 2019; accepted May 21, 2019. Date of publication May 24, 2019; date of current version January 20, 2020. This work was supported in part by the Slovenian Research Agency under Core Research Grant P2-0232 and under Research Grants J2-5473, J7-6781, J2-7211, J2-8173, and L3-4255, and in part by the Brain Aneurysm Foundation, Timothy P. Susco Chair of Research, Research Grant, and in part by the UCLA Radiology Exploratory Research Grant. (Corresponding author: Žiga Špiclin.)

T. Jerman, F. Pernuš, and B. Likar are with the Faculty of Electrical Engineering, University of Ljubljana.

A. Chien is with the Department of Radiology, UCLA Medical School.

Ž. Špiclin is with the Faculty of Electrical Engineering, University of Ljubljana, SI-1000 Ljubljana, Slovenia (e-mail: ziga.spiclin@fe.uni-lj.si).

Digital Object Identifier 10.1109/TBME.2019.2918921

I. INTRODUCTION

INTRACRANIAL aneurysms, a common cerebrovascular pathology with estimated prevalence of 3–5% of the population, are formed when a weakened cerebral arterial wall dilates into a balloon-like structure. Eventually, an aneurysm may rupture, leading to subarachnoid hemorrhage, a serious health condition with a high mortality rate [1], [2]. Several studies [3]–[5] established that morphologic features, such as aneurysm size, neck width, aspect ratio, size ratio, and others [6]–[10] may represent important predictors of the risk of rupture, further growth, and selection of the best treatment time and option, e.g. clipping, coiling or even no treatment with regular follow-up assessment. Furthermore, hemodynamic factors are also implicated in the progression and rupture of intracranial aneurysms [11], [12]. Because of its increasing importance in clinical decision-making processes [13], with potential impact on treatment outcome and patient condition, the aneurysm morphology needs to be assessed from angiographic images as accurately and reliably as possible.

Simple morphologic features like the aneurysm size are routinely extracted from 2D digital subtraction angiography (DSA), 3D DSA, computed tomography angiography (CTA), or magnetic resonance angiography (MRA) images. The aneurysm size, defined as the largest diameter of the aneurysm dome, is a well-established rupture risk factor [1]. Recently, Chien *et al.* [14] showed that nonsphericity index and size ratio at baseline can identify morphological differences between stable and growing aneurysms and can thus be used as surrogate measures of rupture risk. However, even determining the largest aneurysm diameter manually is difficult and subject to high inter- and intra-rater variability as it is generally based on visualization of the aneurysm in 2D, where relevant 3D morphologic information may be obscured and aneurysm asymmetries and vascular occlusions may interfere with the measurement process [15]. Conversely, advanced analysis of an angiographic image involving automated vessel tree segmentation and aneurysm isolation from the parent vessel could result in more accurate and reliable values of such simple morphologic features, or in even more information-rich and clinically useful shape descriptors that otherwise are difficult or impossible to determine manually.

Automated vessel tree segmentation was extensively studied and several methods were developed to handle the common angiographic modalities [16]. Our previous work involved vessel and aneurysm enhancement [17], [18], which also allows

for a good vessel tree segmentation simply by thresholding the enhanced angiogram. The following task is to isolate the aneurysm, which is rather challenging due to high variability of aneurysm sizes and shapes, and parent vessel geometries. Because aneurysm isolation has a direct impact on the accuracy and reliability of the morphologic features, and indirectly also on the computation of hemodynamic features, and because of the deficiencies of state-of-the-art automated methods the aneurysm isolation is in focus of this work.

A. Background

In current clinical practice, assessment of aneurysm's morphology from 3D angiographic images is based on a manually positioned cutting plane (MCP), which isolates the aneurysm from its parent vessel [6], [7], [19]. An alternative to the MCP is to manually outline the aneurysm neck curve by interactive localization and interconnection of landmarks on the vasculature surface mesh. Besides being too tedious and time consuming for routine clinical practice, such a contouring approach was found to exhibit high inter- and intra-rater variability, especially in cases of low-curvature surfaces of the aneurysm neck [20]. Hence, although the planar neck curve determined by MCP is unable to precisely outline the aneurysm's neck, the substantially lower degree-of-freedom (i.e. less reference points) required for positioning the MCP currently makes MCP the preferable technique to isolate aneurysms of various shapes and sizes.

An alternative approach to MCP to obtain neck delineating curves is to employ automated or semi-automated computer-aided methods [21]–[28]. Several methods [21], [23], [27] first model the parent vessels, which have a simpler shape than vascular abnormalities, and then *subtract* the obtained model to isolate the aneurysm. In cases when the aneurysm is elongated, resembling a normal vessel, or when the aneurysm's inlet is similar or larger than the cross-section of the vessel, these methods generally require manual initialization of the parent vessel centerlines or its endpoints in order to constrain the parent vessel model not to run through the aneurysm.

More recent methods focus on extracting the neck curve directly from the vessel tree surface model. For instance, Sgouritsa *et al.* [25] separated the aneurysm's surface from that of the parent vessel using an s-t graph-cut approach. Mohamed *et al.* [24] used a 3D deformable contour constrained by surface's Gaussian curvature, while Cardenes *et al.* [26] computed a geodesic curve using Voronoi regions on the surface mesh as a topologic restriction. Ford *et al.* [22], and Piccinelli *et al.* [28] identified vessel centerlines and clipping points using 3D Voronoi diagrams of the segmented vasculature, from which they then reconstructed and subtracted parent vessel tube surface to isolate the aneurysm. For an accurate and reliable isolation, however, the aneurysm neck curve should be carefully regularized in order to reject implausible curves, mainly at low-curvature surfaces.

Often the obtained neck curve is further regularized by an *ad hoc* solution, which constrains the neck curve to lie in a plane. Mohamed *et al.* [24] and Sgouritsa *et al.* [25] fitted a planar ellipse model to the delineated neck curve, while Piccinelli

et al. [28] fitted a plane so as to extract a planar neck curve. In these methods, the accuracy of the (inherent) cutting plane positioning is limited by the often poor performance of neck curve delineation.

To the best of our knowledge, none of the state-of-the-art methods attempted to fit a cutting plane directly to the vascular surface mesh, which would mimic the neck curve extraction performed manually in clinical routine. Such an approach is also promoted by the results of a recent comparative validation of automated methods by Cardenes *et al.* [20], who compared neck curves obtained by two automatic aneurysm isolation methods [26], [27] and MCP to a reference neck curve, obtained as an average of multiple manually outlined neck curves. Quantitative validation on one synthetic and 26 real aneurysms showed that on average the MCP method resulted in a neck curve more similar to the reference than the neck curves obtained by the two automatic methods. This finding is somewhat surprising since MCP assumes a planar neck curve, which is not generally the case, but seems to be sufficient and effective for clinical purposes. A further motivation is the widespread use of cutting plane based measures in the clinical guidelines for management of intracranial aneurysms [13].

B. Contribution

In this paper, we propose a novel method for automated cutting plane (ACP) positioning based on the detection of certain geometric descriptors of the aneurysm and its parent vasculature. The method is focused on saccular-type of aneurysm and is angiographic modality-agnostic, since its input is only the surface mesh of the aneurysm and its parent vessels.

The proposed method was evaluated and compared to the MCP and manual neck curves positioned by two expert clinicians on 55 cases of intracranial aneurysms. Validation based on average inter-curve distances and comparison of four morphologic features of aneurysms isolated by ACP and MCP demonstrated a very good agreement between the respective two methods. This finding was further confirmed by expert clinicians through qualitative analysis of ACPs with respect to the vascular surface model. Interestingly, intra- and inter-rater variability analysis showed higher neck curve and feature value variabilities for the manual neck curves compared to the MCP. Because the proposed method mimics the intuition behind MCP, enables fast re-evaluation and yields accurate, reliable and consistent aneurysm neck curves, it appears suitable to be introduced into clinical practice.

II. METHOD

Aneurysm isolation method inputs a triangulated surface mesh of the aneurysm and surrounding vasculature and is based on a cutting plane, which is automatically positioned by using certain reference geometric descriptors of the aneurysm and its parent vessel. Namely, the aneurysm's center and centerline determine the aneurysm's principal orientation, a vector originating near the center and pointing in direction of the centerline. This vector is a good initial estimate of the cutting plane's normal, from which the plane's pose is further refined

through domain-specific geometric constraints. Hence, the proposed method consists of four main steps:

- A. Extraction of parent vessel centerlines (Section II-A),
- B. Localization of the aneurysm center (Section II-B),
- C. Identification of the principal orientation (Section II-C).
- D. Positioning of the cutting plane (Section II-D).

The method is angiographic modality-agnostic, since it builds on a triangulated vascular surface mesh, defined by vertices and faces $\mathcal{M} = \{\{\mathbf{x}_m\}, \{\mathbf{f}_n\}; m = 1, \dots, N_M, n = 1, \dots, N_F\}$, that is readily extracted from a 3D cerebral angiography image. The three steps, described in the following subsections, therefore derive information solely from the surface mesh \mathcal{M} .

A. Parent Vessel Centerline

A vessel centerline may be defined as the path connecting centers of vessel's cross-sections, which are generally close to circular except in the vicinity of an aneurysm. The aneurysm thus renders the automatic parent vessel centerline extraction rather difficult.

A novel centerline extraction approach that is not based on the common analysis of cross-sections was developed. In brief, locations of parent vessel's endpoints and their corresponding radii were first determined. Second, pairs of endpoints were connected by the weighted shortest path through vasculature using the fast marching algorithm [29] to define final parent vessel centerlines. The approach is described step by step in the following subsections.

1) Detection of Centerline Endpoints: For a robust estimation of the parent vessel's endpoints we applied an accumulator based solution similar to the Hough transform. Namely, an exhaustive sampling of possible parent vessel's centers was performed such that several candidate endpoints were obtained. For each vertex $\mathbf{x}_m = (x, y, z)$ on mesh \mathcal{M} , a ray was casted in the direction opposite to the surface normal, i.e. $-\mathbf{n}_M$. If the ray intersected the mesh, then the vertex $\mathbf{x}_{m'}$ closest to the intersection and \mathbf{x}_m (Fig. 1(a)) determined a candidate vessel center point \mathbf{x}_v , which was positioned at a distance $r_v = |\mathbf{x}_m - \mathbf{x}_{m'}|/2$ from \mathbf{x}_m . The point \mathbf{x}_v was retained only if the surface normals $\mathbf{n}_M(\mathbf{x}_m)$ and $\mathbf{n}_M(\mathbf{x}_{m'})$ were approximately collinear, according to $|\mathbf{n}_M(\mathbf{x}_m) \circ \mathbf{n}_M(\mathbf{x}_{m'})| > 0.95$. Threshold of 0.95 was empirically determined. This resulted in N_V candidate vessel center points: $\mathcal{V} = \{\mathbf{x}_v; v = 1, 2, \dots, N_V\}$ (Fig. 1(b)).

The candidate vessel center points \mathcal{V} and their corresponding radii r_v were used to construct an accumulator array A_E . The A_E is a discretized 3D space (Fig. 1(c)) with its size equal to the bounding box of the aneurysm mesh \mathcal{M} . All values in the A_E were initially set to zero and, for each candidate vessel center point $\mathbf{x}_v \in \mathcal{V}$, a 3D Gaussian $\mathcal{G}(\mathbf{x}_v; \sigma) = (2\pi\sigma^2)^{-3/2} \exp(-\mathbf{x}_v^T \mathbf{x}_v / 2\sigma^2)$ with a standard deviation $\sigma = r_v/2$ and centered at \mathbf{x}_v was added to the A_E :

$$A_E(\mathbf{x}) = \sum_{v=1}^{N_V} \mathcal{G}(\mathbf{x}_v - \mathbf{x}; r_v/2). \quad (1)$$

Local maxima of $A_E(\mathbf{x})$ yielded a set of candidate centerline endpoints \mathbf{x}_l (Fig. 1(c)), which was reduced to a set of centerline

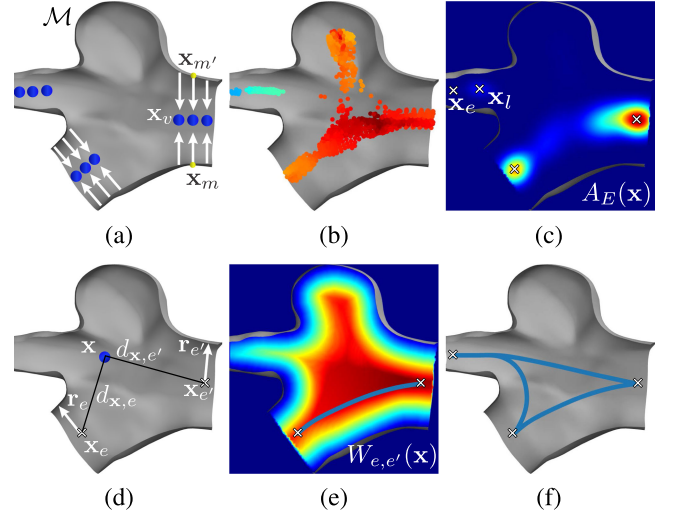


Fig. 1. Extraction of parent vessel endpoints: (a) paired surface normals, (b) halfway locations \mathbf{x}_v color coded according to radii, and (c) endpoint accumulator array. Extraction of parent vessel centerlines: (d) parent vessel radii $r_e, r_{e'}$ at $\mathbf{x}_e, \mathbf{x}_{e'}$ and corresponding distances $d_{\mathbf{x},e}, d_{\mathbf{x},e'}$ to \mathbf{x} , (e) distance weighting array (Eq. (2)), (f) resulting centerlines.

endpoints $\mathcal{E} = \{\mathbf{x}_e; e = 1, 2, \dots, N_E\}$ by retaining exactly one unique point for each of the N_E parent vessel branches. The N_E was set to the number of detected holes in the surface mesh \mathcal{M} [30]. The Points \mathcal{E} were selected as the local maxima closest to the vessel inlets, i.e. vessel sections where the mesh was dissected from the vasculature. To each \mathbf{x}_e a radius r_e was assigned as the radii r_v of the point \mathbf{x}_v closest to \mathbf{x}_e (Fig. 1(d)).

2) Extraction of Centerlines: For each of the $N_E(N_E - 1)/2$ pairs of endpoints $\{\{\mathbf{x}_e, \mathbf{x}_{e'}\}; \mathbf{x}_e \neq \mathbf{x}_{e'} \in \mathcal{E}\}$ with corresponding radii $\{r_e, r_{e'}\}$, a weighting distance array $W_{e,e'}(\mathbf{x})$ (Fig. 1(e)) of the same size as the accumulator array A_E was created:

$$W_{e,e'}(\mathbf{x}) = \min(D_{\mathcal{M}}(\mathbf{x}), r_{e,e'}(\mathbf{x})), \quad (2)$$

where $D_{\mathcal{M}}$ is the distance transform from mesh points \mathcal{M} and has nonzero values only inside the mesh, $r_{e,e'}(\mathbf{x}) = \alpha r_e + (1 - \alpha)r_{e'}$, $\alpha = d_{\mathbf{x},e'}/(d_{\mathbf{x},e} + d_{\mathbf{x},e'})$, and $d_{\mathbf{x},e}$ and $d_{\mathbf{x},e'}$ are the distances between \mathbf{x} and the corresponding endpoints, respectively (Fig. 1(d)). Equation (2) ensures a constant centerline path weight at n-furcations and aneurysm inlets.

Using the fast marching algorithm [29] and values of the array $W_{e,e'}(\mathbf{x})$ as weights, a centerline $\mathcal{P}_{e,e'}$ connecting \mathbf{x}_e and $\mathbf{x}_{e'}$ (Figure 1(e)) was obtained for each pair of endpoints resulting in a set of all parent vessel centerlines \mathcal{P} composed of $N_E(N_E - 1)/2$ individual centerlines (Figure 1(f)).

B. Aneurysm Center

Since saccular intracranial aneurysms are balloon-like dilations of the vessel wall, the development of aneurysm center localization was based on the assumption that at least a part (e.g. apex) of the aneurysm surface is approximately spherical. Consequently, its center \mathbf{x}_A can be established by the least-squares intersection of three vectors, which originate on the

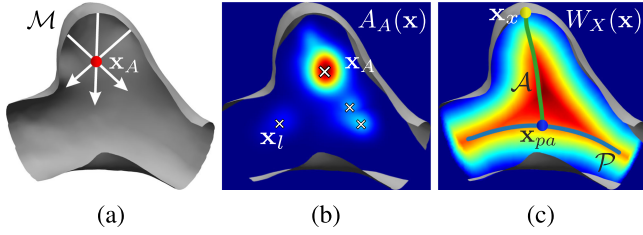


Fig. 2. Localization of aneurysm center: (a) intersections of surface normal triplets, and (b) accumulator array. (c) Extraction of aneurysm centerline \mathcal{A} from apex \mathbf{x}_x to point on the centerline \mathbf{x}_{pa} guided by weight array $W_X(x)$.

triangulated surface mesh \mathcal{M} and point in the direction opposite to the surface normals \mathbf{n}_M (Fig. 2(a)).

For a robust estimation of the aneurysm center an accumulator based approach similar to the parent vessel endpoint detection was used. Random sampling of $N_T = 10^5$ triplets of surface normals was performed such that several candidate center points $\mathcal{C} = \{\mathbf{x}_c; c = 1, 2, \dots, N_C\}$ were obtained. The candidate center points \mathcal{C} and their corresponding distances $d_{c,M}$ to the nearest vertex \mathbf{x}_m on the surface mesh were used to construct an accumulator array A_A , which was initialized to zero and updated as:

$$A_A(\mathbf{x}) = \sum_{c=1}^{N_C} \mathcal{G}(\mathbf{x}_c - \mathbf{x}; d_{c,M}/2). \quad (3)$$

The center of a perfectly spherical aneurysm can be simply obtained by locating the global maximum of the accumulator, i.e. $\arg\max_{\mathbf{x}} A_A(\mathbf{x})$. However, the assumption of perfect sphericity of the mesh forming the aneurysm surface generally does not hold, because the spherical tip of smaller aneurysms is represented by a very small fraction of patches. Hence, instead of a global maximum we extracted the local maxima \mathbf{x}_l in the accumulator (Fig. 2(b)) and selected the aneurysm center \mathbf{x}_A as \mathbf{x}_l with the largest distance from centerlines \mathcal{P} .

C. Aneurysm's Principal Orientation

Similarly to the extraction of the parent vessel centerlines, the aneurysm centerline \mathcal{A} was computed using the fast marching algorithm as the shortest path from the aneurysm apex to the centerlines \mathcal{P} (Fig. 2(c)). The aneurysm apex \mathbf{x}_x was found as the point on the mesh $\mathbf{x}_x \in \mathcal{M}$ most distant from \mathcal{P} . To impose the shortest path to follow through the central sections of the aneurysm the search was weighted by the distance from the mesh: $W_X(\mathbf{x}) = D_M$. The resulting centerline is limited by \mathbf{x}_x and \mathcal{P} , where point \mathbf{x}_{pa} denotes the intersection between \mathcal{A} and \mathcal{P} .

At any given point $z \in [0, 1]$ with step dz across the parametrized curve $\mathcal{A}(z)$ from \mathbf{x}_{pa} to \mathbf{x}_x an aneurysm principal orientation \mathbf{n}_A can be computed as the direction between consecutive curve points, i.e. $\tilde{\mathbf{n}}_A = \mathcal{A}(z + dz) - \mathcal{A}(z)$, $\mathbf{n}_A = \tilde{\mathbf{n}}_A / |\tilde{\mathbf{n}}_A|$.

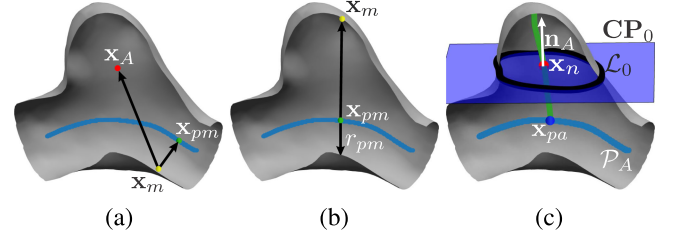


Fig. 3. Geometric terms for extraction of cutting plane \mathcal{CP} : (a) incurvation at \mathbf{x}_m (Eq. (4)) and (b) distance to closest centerline at \mathbf{x}_m (Eq. (5)). (c) Aneurysm principal orientation \mathbf{n}_A and aneurysm center \mathbf{x}_A define the initial \mathcal{CP}_0 . Neck curve \mathcal{L}_0 is the intersection between \mathcal{CP}_0 and the surface mesh.

D. Cutting Plane Positioning

A cutting plane should separate the aneurysm from its parent vessel at locations, where the vessel starts to deform from its normal tubular shape. To find the cutting plane, a novel cost function was developed and minimized using a robust, multistart optimization framework [31].

1) Cost Function: Using the extracted aneurysm center and parent vessel centerline an incurvation $C_i(\mathbf{x}_m)$ (Fig. 3(a)) and distance $C_d(\mathbf{x}_m)$ (Fig. 3(b)) values were assigned to each vertex \mathbf{x}_m as follows:

$$\text{incurvation: } C_i^*(\mathbf{x}_m) = (\mathbf{x}_A - \mathbf{x}_m) \circ (\mathbf{x}_{pm} - \mathbf{x}_m), \quad (4)$$

$$\text{distance: } C_d^*(\mathbf{x}_m) = (|\mathbf{x}_m - \mathbf{x}_{pm}| - r_{pm}), \quad (5)$$

where \mathbf{x}_{pm} was a point on one of the parent centerlines \mathcal{P} , which was closest to \mathbf{x}_m . Radius of the parent vessel r_{pm} at \mathbf{x}_{pm} was computed as the value r_v of the point \mathbf{x}_v (cf. II-A1) closest to \mathbf{x}_{pm} . Incurvation of a point on the surface mesh was computed as the dot product between vectors pointing from \mathbf{x}_m to \mathbf{x}_A and \mathbf{x}_{pm} , and penalizes parts of the aneurysm above the aneurysm center or those below the centerline. Because of mesh and centerline discretization, the values of $C_i^*(\mathbf{x}_m)$ and $C_d^*(\mathbf{x}_m)$ were averaged across several small random perturbations of \mathcal{P} to obtain smooth and continuous values across the mesh. As attempted by definition, C_i^* and C_d^* exhibit low values for points located around the base of the aneurysm as illustrated in Figs. 4(a) and 4(c), respectively.

To achieve comparable contributions of C_i^* and C_d^* , and avoid bias due to varying aneurysm shapes and sizes, C_i^* and C_d^* were first normalized to the range between zero and one, followed by nonlinear scaling to emphasize differences between low and high values:

$$C_i(\mathbf{x}_m) = S\left(\frac{C_i^*(\mathbf{x}_m) - \min C_i^*(\mathbf{x}_m)}{\max C_i^*(\mathbf{x}_m) - \min C_i^*(\mathbf{x}_m)}; \mu_i, p_i\right), \quad (6)$$

$$C_d(\mathbf{x}_m) = S\left(\frac{C_d^*(\mathbf{x}_m)}{\max C_d^*(\mathbf{x}_m)}; \mu_d, p_d\right), \quad (7)$$

where $\min(\cdot)$ and $\max(\cdot)$ were applied over all points $\mathbf{x}_m \in \mathcal{M}$, and $S(x; \mu, p)$ was a sigmoid-like function:

$$S(x; \mu, p) = 1 - \exp\left(-\frac{x^p}{2\mu^p}\right); 0 \leq x \leq 1, \quad (8)$$

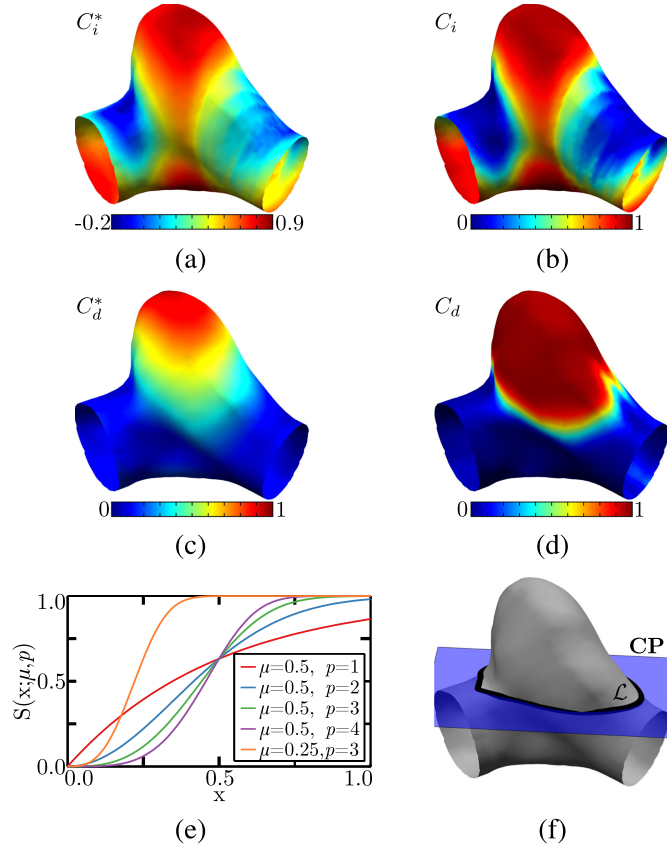


Fig. 4. Responses of geometric terms for cutting plane extraction: (a) non-saturated C_i^* and (b) saturated C_i incursions, and (c) non-saturated C_d^* and (d) saturated C_d distances. (e) Saturation function $S(x; \mu, p)$ for different values of μ and p . (f) Optimal cutting plane and corresponding neck curve.

which saturates values below μ towards zero and those above μ to one. The degree of saturation is controlled by parameter p , where a higher value of p causes more progressive saturation. The influence of parameters μ and p is illustrated in Fig. 4(e), whereas Fig. 4.a-d show C_i and C_d values without and with applying saturation, respectively. For the purpose of cutting plane extraction, μ_i and μ_d were empirically set to 0.5 and 0.25, respectively, while p_i and p_d were set to 3.

Every cutting plane \mathbf{CP} defines a neck curve \mathcal{L} , which is simply the intersection between \mathbf{CP} and \mathcal{M} resulting in a set of surface points $\mathcal{L} = \{\mathbf{x}_m : \mathbf{x}_m \in \mathcal{M} \cap \mathbf{CP}\}$. With every tentative cutting plane a cost function C_{CP} is associated to values C_i and C_d :

$$C_{CP} = \sum_{\mathbf{x}_m \in \mathcal{L}} C_i(\mathbf{x}_m) + \sum_{\mathbf{x}_m \in \mathcal{L}} C_d(\mathbf{x}_m) + C_l. \quad (9)$$

The term C_l , $C_l = |\mathcal{L}|/|\mathcal{L}_0|$, was the ratio of lengths of curves \mathcal{L} and \mathcal{L}_0 , where \mathcal{L}_0 was the neck curve defined by the initial cutting plane \mathbf{CP}_0 described in point-normal form by \mathbf{x}_A and the normal vector \mathbf{n}_A , which represents the aneurysm principal orientation at point $\mathbf{x}_n \in \mathcal{A}$ closest to \mathbf{x}_A (Fig. 3(c)). Normalization of $|\mathcal{L}|$ by $|\mathcal{L}_0|$ ensures C_l to have values comparable to C_i and C_d and in range between 0 and 1. Furthermore, choosing

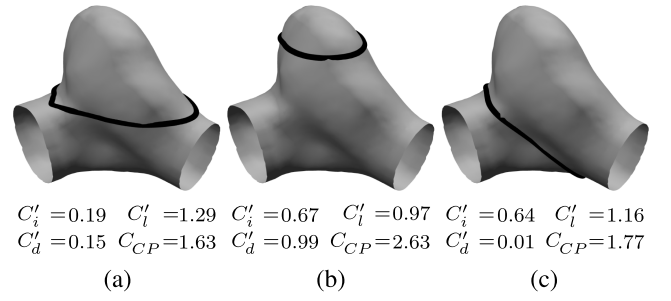


Fig. 5. Aneurysm with three possible neck curves and corresponding values of individual terms of cost function (Eq. (9)). Lower values indicate better cutting plane.

the initial plane to cross through a well defined point in the middle of the aneurysm, i.e. the aneurysm center, provides a stable normalization, while the normalized length term results in neck curves tightly surrounding the aneurysm, i.e. without spurious deviations.

Figure 5 illustrates the impact and interplay of cost terms $C_i' = \sum_{\mathbf{x}_m \in \mathcal{L}} C_i(\mathbf{x}_m)$, $C_d' = \sum_{\mathbf{x}_m \in \mathcal{L}} C_d(\mathbf{x}_m)$, $C_l' = C_l$, and $C_{CP}' = C_i' + C_d' + C_l'$ for three different neck curves positioned on the same aneurysm. A curve distant from the aneurysm base (Fig. 5.b) had high values of C_i' and C_d' resulting in a high combined value C_{CP}' . On the other side, curves closer to the parent vessel had a lower C_{CP}' . Incurvature C_i' was the most segregating factor for rejecting implausible neck curves and had substantially lower values for valid neck curves. The combination of all three cost factors, however, resulted in most robust extraction of the cutting plane (Fig. 5.a).

2) Optimization: Finding the optimal cutting plane was based on minimization of (9) using a multistart framework for global optimization [31]. Despite possible local minima of (9) it was thus possible to find the global minimum of C_{CP}' . Several locations $z \in [0, 1]$ across the aneurysm centerline \mathcal{A} between the point on the parent vessel centerline \mathbf{x}_{pa} (i.e. $\mathcal{A}(z = 0)$) and the approximate aneurysm center \mathbf{x}_n (i.e. $\mathcal{A}(z = 1)$) were used as origins of possible cutting planes. Orientations (θ_{CP}, ϕ_{CP}) were defined in spherical coordinates with respect to aneurysm orientation \mathbf{n}_A ($\mathbf{n}_A \equiv (\theta_{CP} = 0, \phi_{CP} = 0)$) and spanned the space of possible plane normals \mathbf{n}_{CP} . Multiple initial starting points randomly selected over the parameter space $(\theta, \phi, z) \in ([0, \pi/3], [0, 2\pi], [0, 1])$ and followed by a gradient based minimization of (9) determined hypothetical cutting planes. Selecting the parameters corresponding to global minimum determined the optimal cutting plane \mathbf{CP}_{opt} . Finally, a cross-section of the \mathbf{CP}_{opt} with the vascular surface mesh \mathcal{M} yielded the optimal neck curve \mathcal{L}_{opt} (Figure 4(f)).

III. EXPERIMENTS AND RESULTS

A. Datasets

The proposed method for automatic cutting plane positioning and neck curve extraction was evaluated on 55 unruptured intracranial saccular aneurysms with sizes ranging between 2.7 to 20.1 mm and a median size of 6.5 mm. Aneurysms were

extracted from three different modalities that were acquired at two different medical centers.

The first dataset contained 40 aneurysm meshes extracted from 3D CTA images, which were acquired at the Department of Radiological Sciences at Ronald Reagan University of California Los Angeles Medical Center (UCLA dataset). Imaging was based on a standard clinical CTA protocol with matrix size: 512×512 , in-plane pixel size: 0.19–0.41 mm, and slice thickness: 0.6–1.0 mm. The second dataset consisted of 15 aneurysms extracted from 3D CTA, 3D MRA, and 3D DSA images, 5 cases each, acquired at the Neurology Clinic at the University Medical Center Ljubljana (UMCL dataset). The in-plane pixel size for CTA, DSA, and MRA protocols was 0.36–0.42 mm, 0.4 mm, and 0.36 mm, respectively, whereas the corresponding slice thicknesses were 0.4 mm, 0.46 mm, and 0.5 mm. For each acquired volume, first resampled to 0.1 mm isotropic resolution, the aneurysm was manually located and segmented. Then, a marching cubes and smooth-nonshrinking algorithms [32], [33] were applied to the segmentations so as to reconstruct and smooth 3D aneurysm's surface meshes \mathcal{M} , which were used as input to the proposed method.

For evaluation purposes, two trained neuroradiologist individually positioned a manual cutting plane (i.e. the MCP method) which was used to extract a reference neck curve. Both neuro-radiologist also positioned a manual reference curve by placing a series of interconnected points on the mesh (i.e. the MCU method). The process was repeated to gather a second set of manual curves, totalling in four MCP and four MCU curves for each aneurysm case. Prior to each MCU/MCP positioning the order of aneurysms and the initial viewing angle were randomized to reduce recall effects. Automatic aneurysm neck curves were determined by the proposed ACP method.

After isolating the aneurysm with a neck curve, morphologic features were automatically computed following the definitions in the literature [6]–[10]. Since the MCP was a reference for our selected neck curve model, the neck curves and morphologic features obtained with the ACP should be as similar as possible to those obtained by the MCP.

B. Validation Using Inter-Curve Distance

Differences between neck curves obtained by ACP and MCP were evaluated using the average inter-curve distance (AICD), a curve-based measure proposed by Cardenes *et al.* [20]. To compute AICD, automatically and manually defined respective neck curves $\mathcal{L}_{ACP}(s)$ and $\mathcal{L}_{MCP}(s)$ were first parametrized using $s \in [0, 1]$ and unit length. The starting points at $s = 0$ were chosen as the closest points, i.e. $\min |\mathcal{L}_{MCP}(0) - \mathcal{L}_{ACP}(0)|$, while the remaining curve points were sampled such that the orientation of both curves was consistent. Based on parametrized ACP and MCP curves, the AICD was computed as:

$$AICD = \left(\frac{2}{|\mathcal{L}_{MCP}| + |\mathcal{L}_{ACP}|} \right) \sum_{s=0}^1 |\mathcal{L}_{MCP}(s) - \mathcal{L}_{ACP}(s)|, \quad (10)$$

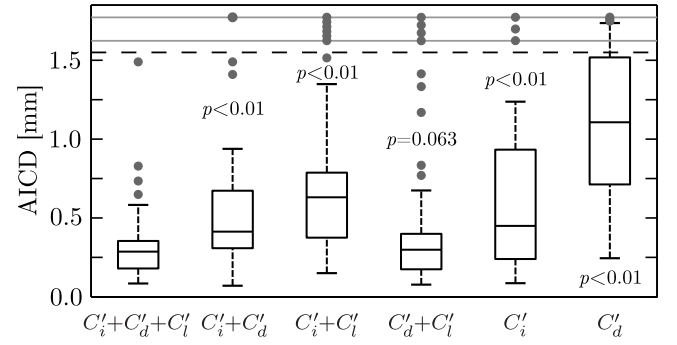


Fig. 6. Box-whisker plots of average inter-curve distance (AICD) between manually and automatically positioned cutting planes across 55 aneurysms cases. Besides the final cost function C_{CP} (9) (i.e. left), the average AICD is shown for various combinations of cost terms C'_i , C'_d , and C'_l . The p -values were computed with respect to C_{CP} using Wilcoxon signed-rank test.

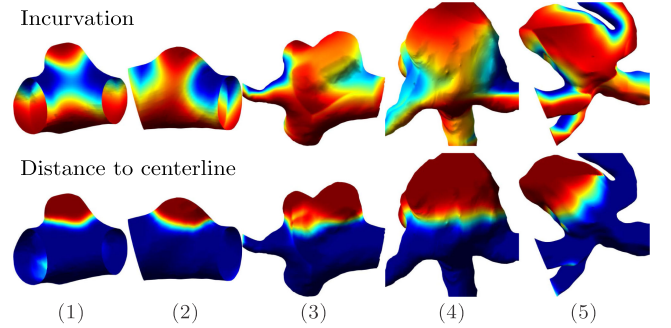


Fig. 7. Incurvation and distance to centerlines for five different aneurysms.

where $|\mathcal{L}_{MCP}|$ and $|\mathcal{L}_{ACP}|$ were MCP and ACP curve lengths, respectively, and $|\mathcal{L}_{MCP}(s) - \mathcal{L}_{ACP}(s)|$ the distance between two corresponding curve points.

Figure 6 shows box-whisker plots of AICD computed between pairs of ACP and MCP defined neck curves. For each of the 55 aneurysms the AICD was averaged over all four manual reference planes (2 MCPs by each of 2 observers). To showcase the influence of each of the three cost terms in (9) on cutting plane optimization, the AICDs obtained by various combinations of these terms were analyzed.

Using only one term resulted in high median values and large interquartile ranges. Adding a second term reduced both the median and interquartile range values. The combination of the distance C'_d and length terms C'_l had a low median AICD of 0.30 mm and interquartile range of 0.22 mm. Compared to the proposed cost function consisting of all three terms, which achieved the best AICD median value of 0.29 mm and interquartile range of 0.17 mm, the difference was close to being significant ($p = 0.063$) according to the Wilcoxon signed rank test [34]. Nevertheless, it follows from the distance terms shown for five aneurysms in Fig. 7 that, while minimizing C'_d favors planes near the parent vessel, the optimal plane could revolve around the vessel instead of the aneurysm's dome because of a low C'_d on vessel sections. Consequently, the combination of

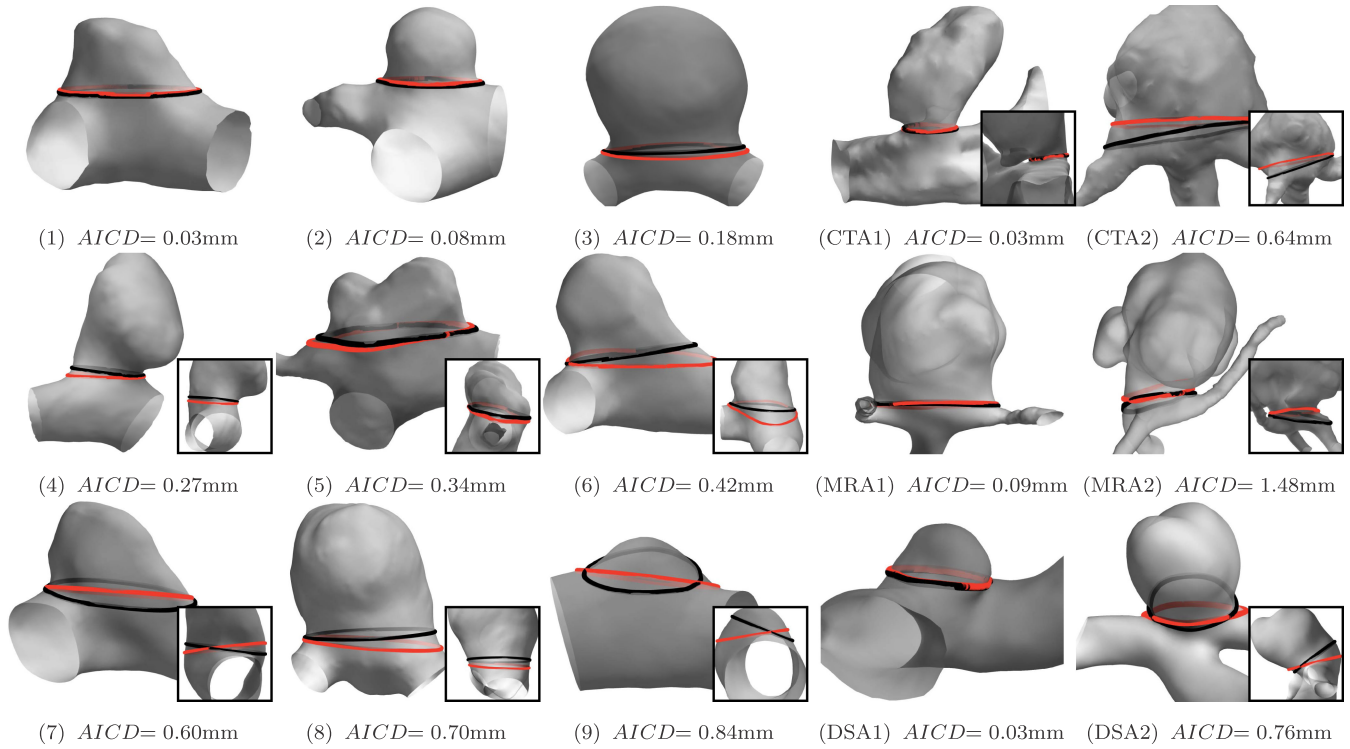


Fig. 8. Fifteen aneurysms superimposed with manually (*red*) and automatically (*black*) extracted neck curves and corresponding average inter-curve distance (AICD). Additional views are shown where this may improve visual assessment.

terms C'_d and C'_l had many outliers. Including the incurvation term C'_i in the proposed cost function (Eq. (9)) anchored the neck curve at the aneurysm base, where the dome meets the parent vessel and where the incurvation has the lowest values by definition (Fig. 7). With the proposed cost function, only one case had AICD higher than 1.0 mm, and 90% of the tested cases achieved an AICD lower than 0.5 mm.

Figure 8 shows side views of neck curves obtained by ACP and MCP on 15 different aneurysms. Aneurysms in Figs. 8. 1–9 are from the UCLA dataset and were selected across the whole range, i.e. lowest to highest value, of obtained AICDs. The other six aneurysms are from the UMCL dataset and show the lowest and highest AICD cases obtained for ACP-MCP comparison for the CTA, DSA, and MRA modalities. When AICD was lower than 0.3 mm the ACP and MCP defined neck curves clearly overlapped. In cases with AICD > 0.4 mm shown in Figs. 8. 6–9, CTA2, DSA2, MRA2 the ACP and MCP defined neck curves generally differed in their vertical position where the neck is ill defined. The most apparent difference in the plane positioning can be seen in aneurysms 9 and DSA2. The former is very small and without a pronounced neck, thus, positioning can be quite arbitrary. Conversely, the latter is larger and tilted with a bulge around the neck, which might have hindered the neck positioning. The ACP in aneurysm MRA2 was positioned significantly lower than the expected neck curve, which resulted in the highest AICD of all 55 aneurysm and the only one with AICD > 1 mm.

To put into perspective the AICDs between ACPs and MCPs we compared with intra- and inter-observer AICDs computed

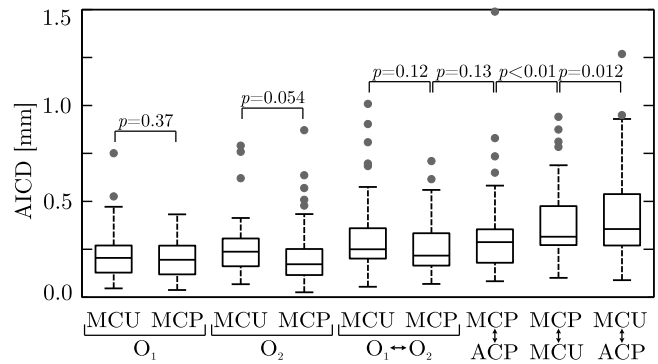


Fig. 9. Average inter-curve distances (AICDs) between manually (MCP) and automatically positioned cutting planes (ACP), and manually placed cutting curves (MCU). For each aneurysm two observers positioned two MCPs and two MCUs each so as to evaluate the intra- (O₁, O₂) and inter-rater (O₁ ↔ O₂) performance. Moreover, a comparison of all obtained MCPs and MCUs with ACPs was conducted. The p-values were computed using a Wilcoxon signed-rank test.

for MCPs and MCUs. Figure 9 shows the resulting box-whisker plots of AICD computed between pairs of manually or automatically defined neck curves. Looking at the individual intra-observer performances, the median values of MCP were generally lower than the median values of MCU. However, for observer O₁ the difference was found insignificant ($p = 0.37$) and on the border of significance ($p = 0.054$) for the second observer O₂. A similar trend was found when comparing AICDs of inter-observer MCUs and MCPs. Furthermore, comparing the

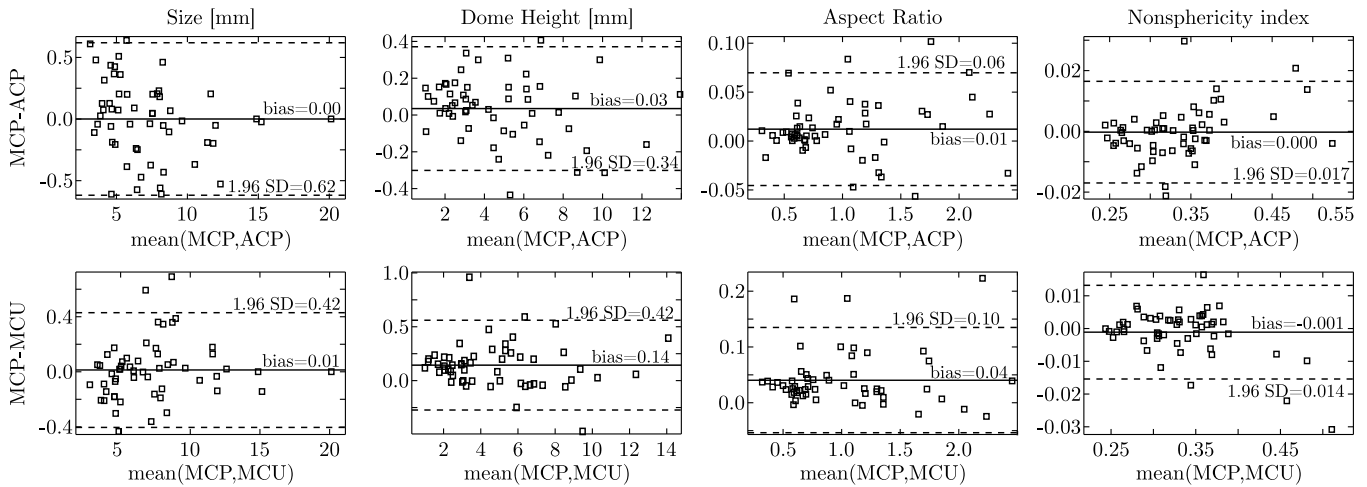


Fig. 10. Bland-Altman diagrams show a good agreement for four different morphologic measurements, obtained for aneurysms isolated with either automatically (ACP) or manually (MCP) positioned cutting planes, or manually positioned cutting curves (MCU).

AICD distributions between ACP and MCP to the MCP based inter-observer variability yielded an insignificant ($p = 0.13$) difference between the two, which affirmed the viability of the proposed method. On the other hand, the AICDs between either MCP or ACP and MCU were significantly higher than the inter-observer AICDs with median values of 0.32 and 0.36, which was expected due to the fundamental difference in the underlying neck curve model. Nevertheless, the difference between ACP or MCP to MCU was still comparable.

C. Validation on Morphologic Features

The goal of aneurysm isolation was to compute morphologic features, which may serve as indicators of rupture risk and also as basis for treatment decisions. We computed four established morphologic features [7], [14]: 1) size (S), 2) dome height (DH), 3) aspect ratio (AR), and 4) nonsphericity index (NSI). Differences between values obtained by the ACP, MCP, and MCU methods and the Bland-Altman plots were used to study the disagreement between the MCP method and the ACP or MCU method.

Bland-Altman diagrams in Fig. 10 show the bias and dispersion (± 1.96 standard deviation limits) of the four morphologic features across 55 aneurysms isolated with MCP, ACP, and MCU. The values of MCP and MCU were averaged across all four manual reference curves. For all four features the bias between MCP and ACP (Fig. 10, upper row) was consistently above zero up to 0.03, which is a negligible under-estimation (i.e. under 1% of the mean measurement value) of the feature values as also observed by visual neck curve comparison (Fig. 8). The 95% confidence levels were between 5.1 and 8%, except for a few aneurysms with AICD higher than 0.7 mm that are shown in Fig. 8. However, for these cases the agreement between ACP and MCP expressed by the morphologic features was still high.

In terms of SD, a similar agreement was found for all morphologic features also when comparing MCP to MCU. On the other hand, the analysis of the biases showed low values for S and NSI features, while there was a high bias for DH that,

by definition, translated also into a high bias in AR. While the dome height is robustly computed for MCP as the shortest distance from the dome apex to the cutting plane, the DH from the apex to manually delineated neck curve (i.e. MCU) is ill-defined and highly affected by the variability in neck delineations. This resulted in high bias for DH and AR features when comparing the MCP and MCU models.

D. Complex Geometries

We consider here the performance of the proposed method in aneurysms with complex geometries, such as aneurysms with multiple lobulations. Such aneurysms will result in multiple local maxima in the accumulator array \mathcal{A}_A , which will be treated as hypothetical aneurysm centers. Among local maxima with the associated accumulator value above 10% of the value corresponding to global maxima, the method selects the position of maximum furthest from the aneurysm centerline. While this is a heuristic strategy, we only require that the aneurysm center is on the correct side of the aneurysm inlet. This is sufficient to get reasonable values for the incurvation feature in Eq. (4). Experiment was performed on an aneurysm with a complex geometry that included five lobulations (smaller sacs). The aneurysm centers were positioned in each of these sacs and, for each center, we computed the neck plane curves using the proposed ACP method. The resulting five neck curves are depicted in Fig. 11. The choice of aneurysm center had a negligible impact on the final positioning of the neck curves.

While the presence of multiple lobulation and second sac is a clear indication of high risk of rupture, our method's primary focus is on small aneurysms (diameter < 7 mm), where the rupture risk is seemingly small and where the decision between "to treat" and "not to treat" is most difficult.

E. Computation Times

The proposed method was implemented in Mathworks Matlab 2015a and was not optimized for speed. All the experiments were conducted on a Intel i7 4770, 3.4 GHz, 32 GB system

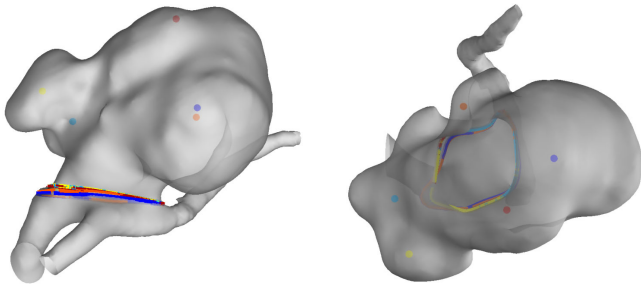


Fig. 11. Five manually selected aneurysm centers and the resulting neck plane curves computed by the ACP method.

memory and Microsoft Windows 7 operating system. Average execution times per aneurysm case were 20 minutes, where most time was spent on cutting plane optimization. The Hough-like feature detectors and the multi-start optimization approach easily lend themselves to massive parallelization using graphics processing units, thus, we expect that the execution times can be shortened by several orders of magnitude.

IV. DISCUSSION

High variability of intracranial aneurysms in terms of shape, size and anatomical location renders the process of their isolation from the parent vessels a very critical step. The isolation needs to be performed consistently to ensure accurate computation of morphologic features used for clinical assessment and decision-making. Thus, this work is focused on aneurysm isolation.

A. Novel Methodology

The proposed aneurysm isolation method is based on certain reference geometric descriptors of the aneurysm and its perivascular structure, which are obtained from the corresponding surface mesh. Each of the reference descriptors such as the aneurysm center, parent vessel endpoints and centerlines were localized using novel Hough-like feature detectors. In general these comprised descriptor accumulation, followed by a multi-hypothesis detection framework that extracted the final descriptor. For the purpose of multi-hypothesis based detection, several novel cost functions were developed by imposing intuitive geometric constraints to each of the descriptors. The use of a two stage approach composed by feature detection and multi-hypothesis selection resulted in highly reliable extraction of geometric descriptors, which served to accurately position the initial aneurysm cutting plane.

Through optimization of a novel cost function, the cutting plane was enforced to intersect the smooth vascular surface mesh at highly incurvating regions and close to the parent vessel, while shorter intersection circumference, i.e. neck curve length, was preferred. These fairly intuitive properties of the aneurysm neck were encoded by corresponding three cost function terms: 1) incurvation, 2) distance from parent vessel, and 3) curve length. The experiments showed that all terms contributed to optimal positioning of the cutting plane (Fig. 6). Among the

three terms, the incurvation contributed most to the accuracy as it prevented the cutting plane to be positioned at implausible locations (like those intersecting with the parent vessel or the apex of aneurysm's dome) and guided the cutting plane positioning towards the aneurysm's base.

The proposed method is based solely on the analysis of a vascular surface mesh. Hence, as long as the vascular surface mesh can be accurately and reliably extracted from the angiogram, a task for which several automated methods were previously developed [16], the proposed method can be used with any 3D angiographic modality. This is verified in the experiments that involved 3D CTA, MRA and DSA datasets from two different sites.

B. Validation and Comparison to State-of-the-Art

Quantitative validation of the proposed automated cutting plane (ACP) positioning method was based on a comparison to a manually defined cutting plane (MCP) on two datasets consisting of 55 intracranial saccular aneurysms acquired from three angiographic modalities. The average inter-curve distance (AICD) between ACP and MCP derived aneurysm neck curves was below 0.29, 0.35 and 0.48 mm in 50%, 75% and 90% of the 55 cases, which indicates high accuracy and robustness of the proposed method. In comparison to the inter-rater positioning of the MCPs (Fig. 9), the proposed method yielded neck curves with comparable AICD, which indicates good agreement with the reference neck curves. Conversely, the AICDs between ACP and manually delineated neck curves (MCU) were higher, as expected due to a fundamental difference in the underlying neck curve model. This was also confirmed by similar AICDs obtained in comparison between MCU and ACP.

Differences in the ACP and MCP derived neck curves were visually assessed by two expert clinicians who established a high overlap between ACP and MCP based curves for AICDs below 0.30 mm, a moderate overlap for AICDs between 0.30 mm and 0.50 mm, a slight misplacement for AICDs between 0.50 mm and 1.0 mm, and a large error of the ACP neck curve for AICDs above 1.0 mm (Fig. 8). The latter appeared only in 1 out of 55 cases, while the slight misplacement could also be detected in four aneurysms. These five aneurysms had poorly defined necks, which also reflected in their higher MCP based inter-rater AICDs. Fig. 8.MRA2 shows the worst performing case where the ACP is pushed rather far towards the parent vessels. In such cases, manual correction could be used to reposition the plane. Nevertheless, the impact of the imperfect cutting plane positioning that resulted in higher AICDs was found to have a negligible effect on the derived morphologic features, because the obtained neck curves differed only slightly in orientation or vertical position. Both clinical experts were satisfied with the automatic plane positioning, provided that consistency in the follow-up positioning can be ensured, a condition more easily satisfied by the proposed ACP than by MCP method.

Several authors evaluated their automated neck delineation methods by comparing various morphologic features to those obtained from manually isolated aneurysms using Bland-Altman diagrams. We followed this approach and demonstrated

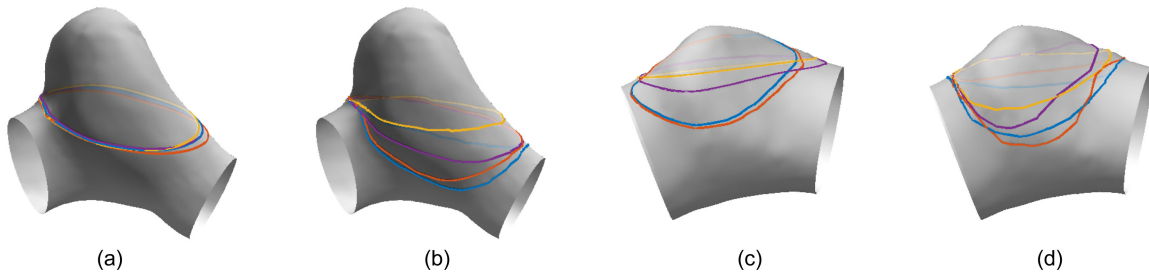


Fig. 12. Inter-rater variability of manually positioned neck planes (a, c) and manual delineations of the neck curves (b, d) for two aneurysms with poorly defined necks. Two raters performed two delineations, which resulted in four neck curves.

a convincing agreement between ACP and MCP derived features, reflected in a rather low bias and standard deviation (SD) for each of the four Bland-Altman diagrams (Fig. 10). Compared to Bland-Altman diagrams for the DH, AR, and NSI features across 26 aneurysm cases obtained using the GTR method [26], the proposed method had lower biases and considerably lower SDs. Namely, Cardenes *et al.* [26] reported the following bias \pm SD values of 0.13 ± 0.41 , 0.04 ± 0.10 , and 0.01 ± 0.02 for DH, AR, and NSI, respectively, whereas the respective values obtained by the proposed method on our set of 55 aneurysm cases were 0.03 ± 0.17 , 0.01 ± 0.03 , and 0.00 ± 0.01 . The proposed method achieved significantly lower SD values for AR (i.e. aspect ratio), which is an established predictor of rupture risk [1], [6], [7].

C. Cutting Plane as Neck Curve Model: Pros and Cons

Isolation based on a cutting plane is simple and effective, however, its potential limitation is the assumption that the neck curve lies in a plane, which generally is not the case. This mainly concerns the neck curve accuracy, thus several researches previously focused on delineating the neck curve directly on the vascular surface mesh and not through positioning of the cutting plane [21]–[28]. The main difficulty with the automated neck curve delineation is to devise a proper regularization that is capable to reject implausible curves, mainly at low-curvature surfaces where positioning is ambiguous. In such situations, even among the clinicians there is currently no consensus about where to place the neck curve, which was confirmed by typically higher inter-curve distances between the same or different observers for manually delineated neck curves compared to manually positioned neck planes (Fig. 8). For both automated and manual approaches this ambiguity is the cause of high variability of neck delineation, which in turn adversely impacts reliability and consistency, both critical especially for aneurysm follow-up. Using the cutting plane thus presents a mean for regularizing the neck curve extraction.

Methods for cutting plane positioning were previously studied [24], [25], [27], [28], but mainly in the context of aneurysm morphologic feature assessment. Most features are defined based on the cutting plane. Certain aneurysm isolation methods used in these studies are based on neck curve delineation, thus to compute the features, a plane was fit to the neck curve or planar neck constraint was applied. This may be a huge pitfall, since

such plane fitting process itself does not take into account the aneurysm and parent vessel morphology. Hence, the fitted plane and the obtained neck curve is suboptimal, which may adversely affect morphologic feature computation. While the curve-based methods could be used for development of new morphologic features, the features currently used in clinical practice and reported in the guidelines for the management of patients with intracranial aneurysms are all based on a cutting plane [13].

Our strategy was a direct positioning of the cutting plane using the vascular surface mesh. The cutting plane may be thought of as a low-degree-of-freedom model of the neck curve, used as an explicit mean to regularize the neck curve extraction.

D. Clinical Application

We primarily focus on the quantification and risk assessment in aneurysms that are eligible for the “no treatment” option with regular imaging follow-up. Such aneurysms are generally small (diameter < 7 mm), with seemingly simple geometry. Note that in our dataset of 55 aneurysms the median dome size was 6.5 mm. The main difficulty with the small aneurysms is that they often lack surface curvature features that would clearly disambiguate the neck position. This issue was clearly highlighted when manually positioning the cutting plane or the neck curve in such aneurysms (Fig. 12). Clearly, neck based isolation is more variable than using a low-degree-of-freedom model such as the cutting plane. During automated cutting plane positioning, several very intuitive geometric descriptors and purposely devised robust detectors of these descriptors were employed so as to ensure reliability and consistency, which was demonstrated by the experiments and results.

Due to the proven clinical usefulness of cutting plane positioning [6]–[10], [35] and established clinical guidelines [13] the proposed method thus has a high potential for immediate integration into a computer-aided system and its introduction into clinical practice.

V. CONCLUSION

A novel method for automatic cutting plane positioning was proposed based solely on the analysis of the vascular surface mesh. The method employs novel Hough-like and multi-hypothesis based methods of aneurysm center, parent vessel inlet centers and centerlines. Based on these the dilations of vascular surface in the form of an aneurysm are identified by

an intuitive, geometry-inspired cost function optimization. The obtained cutting plane is used to isolate the aneurysm's dome from the parent vessel allowing to compute morphologic and hemodynamic features of the aneurysm.

Quantitative and expert evaluation performed on 55 intracranial saccular aneurysms from two sites and 3D DSA, CTA, and MRA angiographic modalities showed small inter-curve distances between neck curves obtained by automatically and manually positioned cutting planes and a good agreement between upon-based morphologic features. To serve as reference for validation, two experts performed repeated manual isolation by placing the MCP and the neck curves. As a side results we found that intra- and inter-rater variability of neck curves and features obtained by manual delineation of the neck curves was higher compared to the MCP, indicating robustness of cutting plane and justifying its use for clinical purposes.

The novel method is angiographic modality agnostic, delivers repeatable isolation important for objective follow-up aneurysm assessment, its performance is comparable to MCP, while re-evaluation in case of obvious failure is fast and simple. The observed low bias and standard deviation of the evaluated four clinically established morphologic features versus MCP-derived ones shows that the automatic cutting plane has a great potential for clinical application.

ACKNOWLEDGMENT

The authors would like to thank V. Lau from UCLA for the help with data collection.

REFERENCES

- [1] N. Etminan and G. J. Rinkel, "Unruptured intracranial aneurysms: Development, rupture and preventive management," *Nature Rev. Neurol.*, vol. 12, no. 12, pp. 699–713, Dec. 2016.
- [2] J. L. Brisman, J. K. Song, and D. W. Newell, "Cerebral aneurysms," *The New England J. Med.*, vol. 355, no. 9, pp. 928–939, Aug. 2006.
- [3] M. Sonobe *et al.*, "Small unruptured intracranial aneurysm verification study SUAVE study, Japan," *Stroke*, vol. 41, no. 9, pp. 1969–1977, Sep. 2010.
- [4] J. P. Villablanca *et al.*, "Natural history of asymptomatic unruptured cerebral aneurysms evaluated at CT angiography: Growth and rupture incidence and correlation with epidemiologic risk factors," *Radiology*, vol. 269, no. 1, pp. 258–265, Oct. 2013.
- [5] R. D. Brown Jr and J. P. Broderick, "Unruptured intracranial aneurysms: Epidemiology, natural history, management options, and familial screening," *Lancet Neurol.*, vol. 13, no. 4, pp. 393–404, Apr. 2014.
- [6] M. L. Raghavan, B. Ma, and R. E. Harbaugh, "Quantified aneurysm shape and rupture risk," *J. Neurosurgery*, vol. 102, no. 2, pp. 355–362, Feb. 2005.
- [7] S. Dhar *et al.*, "Morphology parameters for intracranial aneurysm rupture risk assessment," *Neurosurgery*, vol. 63, no. 2, pp. 185–197, Aug. 2008.
- [8] A. Chien, J. Sayre, and F. Viñuela, "Comparative morphological analysis of the geometry of ruptured and unruptured aneurysms," *Neurosurgery*, vol. 69, no. 2, pp. 349–356, Aug. 2011.
- [9] D. Kashiwazaki and S. Kuroda, "Size ratio can highly predict rupture risk in intracranial small (5 mm) aneurysms," *Stroke*, vol. 44, no. 8, pp. 2169–2173, Aug. 2013.
- [10] M. Rahman *et al.*, "Size ratio correlates with intracranial aneurysm rupture status," *Stroke*, vol. 41, no. 5, pp. 916–920, May 2010.
- [11] J. R. Cebral *et al.*, "Efficient pipeline for image-based patient-specific analysis of cerebral aneurysm hemodynamics: Technique and sensitivity," *IEEE Trans. Med. Imag.*, vol. 24, no. 4, pp. 457–467, Apr. 2005.
- [12] D. M. Sforza, C. M. Putman, and J. R. Cebral, "Hemodynamics of cerebral aneurysms," *Annu. Rev. Fluid Mechanics*, vol. 41, no. 1, pp. 91–107, 2009.
- [13] B. G. Thompson *et al.*, "Guidelines for the management of patients with unruptured intracranial aneurysms: A guideline for healthcare professionals from the american heart association/american stroke association," *Stroke*, vol. 46, pp. 2368–2400, 2015.
- [14] A. Chien *et al.*, "Nonsphericity index and size ratio identify morphologic differences between growing and stable aneurysms in a longitudinal study of 93 cases," *Amer. J. Neuroradiol.*, vol. 39, no. 3, pp. 500–506, 2018.
- [15] F. Kucukay *et al.*, "Three-dimensional volume rendering digital subtraction angiography in comparison with two-dimensional digital subtraction angiography and rotational angiography for detecting aneurysms and their morphological properties in patients with subarachnoid hemorrhage," *Eur. J. Radiol.*, vol. 81, no. 10, pp. 2794–2800, Oct. 2012.
- [16] D. Lesage *et al.*, "A review of 3D vessel lumen segmentation techniques: Models, features and extraction schemes," *Med. Image Anal.*, vol. 13, no. 6, pp. 819–845, Dec. 2009.
- [17] T. Jerman *et al.*, "Blob enhancement and visualization for improved intracranial aneurysm detection," *IEEE Trans. Vis. Comput. Graph.*, vol. 22, no. 6, pp. 1705–1717, Jun. 2016.
- [18] T. Jerman *et al.*, "Enhancement of vascular structures in 3D and 2D angiographic images," *IEEE Trans. Med. Imag.*, vol. 35, no. 9, pp. 2107–2118, Sep. 2016.
- [19] B. Ma, R. E. Harbaugh, and M. L. Raghavan, "Three-dimensional geometrical characterization of cerebral aneurysms," *Ann. Biom. Eng.*, vol. 32, no. 2, pp. 264–273, Feb. 2004.
- [20] R. Cardenes *et al.*, "Performance assessment of isolation methods for geometrical cerebral aneurysm analysis," *Med. Biol. Eng. Comput.*, vol. 51, no. 3, pp. 343–352, Mar. 2013.
- [21] W. C. K. Wong and A. C. S. Chung, "Augmented vessels for quantitative analysis of vascular abnormalities and endovascular treatment planning," *IEEE Trans. Med. Imag.*, vol. 25, no. 6, pp. 665–684, Jun. 2006.
- [22] M. D. Ford *et al.*, "An objective approach to digital removal of saccular aneurysms: Technique and applications," *The Brit. J. Radiol.*, vol. 82, no. special_issue_1, pp. S55–S61, Jan. 2009.
- [23] D. G. Kang, D. C. Suh, and J. B. Ra, "Three-dimensional blood vessel quantification via centerline deformation," *IEEE Trans. Med. Imag.*, vol. 28, no. 3, pp. 405–414, Mar. 2009.
- [24] A. Mohamed *et al.*, "Computer-aided planning for endovascular treatment of intracranial aneurysms (CAPETA)," in *Proc. SPIE, Medical Imaging 2010: Visualization, Image-Guided Procedures, and Modeling*, K. H. Wong and M. I. Miga, Eds., San Diego, CA, USA, vol. 7625, 2010, pp. 762532–762539, doi: [10.1117/12.841042](https://doi.org/10.1117/12.841042).
- [25] E. Sgouritsa *et al.*, "Neck localization and geometry quantification of intracranial aneurysms," in *Proc. IEEE Int. Symp. Biomed. Imag., From Nano Macro*, Apr. 2010, pp. 1057–1060.
- [26] R. Cardenes *et al.*, "Automatic aneurysm neck detection using surface Voronoi diagrams," *IEEE Trans. Med. Imag.*, vol. 30, no. 10, pp. 1863–1876, Oct. 2011.
- [27] I. Larrabide *et al.*, "Three-dimensional morphological analysis of intracranial aneurysms: A fully automated method for aneurysm SAC isolation and quantification," *Med. Phys.*, vol. 38, no. 5, pp. 2439–2449, May 2011.
- [28] M. Piccinelli *et al.*, "Automatic neck plane detection and 3d geometric characterization of aneurysmal sacs," *Ann. Biomed. Eng.*, vol. 40, no. 10, pp. 2188–2211, Oct. 2012.
- [29] T. Deschamps and L. D. Cohen, "Fast extraction of minimal paths in 3d images and applications to virtual endoscopy," *Med. Image Anal.*, vol. 5, no. 4, pp. 281–299, 2001.
- [30] W. Zhao, S. Gao, and H. Lin, "A robust hole-filling algorithm for triangular mesh," *The Vis. Comput.*, vol. 23, no. 12, pp. 987–997, 2007.
- [31] Z. Ugray *et al.*, "Scatter search and local NLP solvers: A multistart framework for global optimization," *INFORMS J. Comput.*, vol. 19, no. 3, pp. 328–340, 2007.
- [32] W. E. Lorensen and H. E. Cline, "Marching cubes: A high resolution 3D surface construction algorithm," in *Proc. 14th Annu. Conf. Comput. Graph. Interactive Techn.*, 1987, pp. 163–169.
- [33] J. R. Cebral and R. Löhner, "From medical images to anatomically accurate finite element grids," *Int. J. Numer. Methods Eng.*, vol. 51, no. 8, pp. 985–1008, Jul. 2001.
- [34] F. Wilcoxon, "Individual comparisons by ranking methods," *Biometrics Bull.*, vol. 1, no. 6, pp. 80–83, Dec. 1945.
- [35] A. Chien and J. Sayre, "Morphologic and hemodynamic risk factors in ruptured aneurysms imaged before and after rupture," *Amer. J. Neuroradiol.*, vol. 35, no. 11, pp. 2130–2135, Nov. 2014.